Exploring the pH dependence of an improved PETase

Cyril Charlier, Sabine Gavalda, Jelena Grga, Laura Perrot, Valeria Gabrielli, Frank Löhr, Julia Schörghuber, Roman Lichtenecker, Grégory Arnal, Alain Marty, et al.

▶ **To cite this version:**

Cyril Charlier, Sabine Gavalda, Jelena Grga, Laura Perrot, Valeria Gabrielli, et al.. Exploring the pH dependence of an improved PETase. Biophysical Journal, In press, 10.1016/j.bpj.2024.04.026 . hal-04569437

HAL Id: hal-04569437
https://cnrs.hal.science/hal-04569437v1

Submitted on 6 May 2024

HAL is a multi-disciplinary open access archive for the deposit and dissemination of scientific research documents, whether they are published or not. The documents may come from teaching and research institutions in France or abroad, or from public or private research centers.

L'archive ouverte pluridisciplinaire **HAL**, est destinée au dépôt et à la diffusion de documents scientifiques de niveau recherche, publiés ou non, émanant des établissements d'enseignement et de recherche français ou étrangers, des laboratoires publics ou privés.

Manuscript

Click here to view linked References

Click here to access/download;Manuscript;manuscript_210424.docx

Exploring the pH dependence of an improved PETase

Cyril Charlier,[1] Sabine Gavalda,[2] Jelena Grga,[1] Laura Perrot,[1] Valeria Gabrielli,[1] Frank Löhr,[3] Julia Schörghuber,[4] Roman Lichtenecker,[4,5] Grégory Arnal, [2] Alain Marty,[2] Vincent Tournier,[2] Lippens Guy[1,*]

[1] Toulouse Biotechnology Institute (TBI), University of Toulouse, CNRS, INRAE, INSA Toulouse, 135 Avenue de Rangueil, 31400 Toulouse Cedex, France

[2] Carbios, Parc Cataroux – Bâtiment B80, 8 rue de la Grolière, 63100 Clermont-Ferrand, France

[3] Institute of Biophysical Chemistry, Center for Biomolecular Magnetic Resonance, Goethe University Frankfurt, 60438 Frankfurt am Main, Germany.

[4] Institute of Organic Chemistry, University of Vienna, Währingerstraße 38, 1090 Vienna, Austria

[5] MAG-LAB, Karl-Farkas-Gasse 22, 1030 Vienna, Austria

*Correspondence to: glippens@insa-toulouse.fr

Running Title : pH dependence of an improved PETase

Abstract

Enzymatic recycling of plastic and especially of polyethylene terephthalate (PET) has shown great potential to reduce its negative impact on our society. PET hydrolases (PETases) have been optimized using rational design and machine learning, but the mechanistic details of the PET depolymerization process remain unclear. Belonging to the carboxylic-ester hydrolase family with a canonical Ser-His-Asp catalytic triad, their observed alkaline pH optimum is generally thought to be related to the protonation state of the catalytic His. Here, we explore this aspect in the context of LCC^{ICCG}, an optimized PETase, derived from the Leaf-branch Compost Cutinase (LCC) enzyme. We use NMR to identify the dominant tautomeric structure of the six histidines. Five show surprisingly low pKa values below 4.0 while the catalytic H242 in the active enzyme displays a pKa value that varies from 4.9 to 4.7 when temperatures increase from 30°C to 50°C. Whereas the hydrolytic activity of the enzyme towards a soluble substrate can be modeled by the corresponding protonation/deprotonation curve, an important discrepancy is found when the substrate is the solid plastic. This opens the way to further mechanistic understanding of the PETase activity, and underscores the importance of studying the enzyme at the liquid/solid interface.

Statement of Significance

Enzymatic plastic biodegradation is a promising avenue to reduce the global burden of plastic waste and thereby limit its global impact on the environment and on human health. Understanding the atomic details of the catalytic mechanisms at the enzyme/plastic interface should help to further improve enzyme performance. Here, we examine the pH dependence of LCC^{ICCG}, an optimized PETase for depolymerization of PET waste at industrial scale. We characterize its six histidines in atomic detail and determine their respective pKa values. Furthermore, we link the pH-dependent catalytic efficiency of the LCC^{ICCG} towards soluble and insoluble PET samples to the protonation state of the catalytic histidine. Our study contributes to the mechanistic understanding of the catalytic behaviour of PETase during PET depolymerization.

Introduction

Enzymes containing a Serine-Histidine-Aspartate catalytic triad can catalyze an amazing number of reactions (1). The mechanism has been studied in exquisite detail by both crystallography and NMR spectroscopy (2) , and involves the attack of the Serine oxygen to form a tetrahedral intermediate with the carbon of the ester bond (Figure 1). The catalytic Histidine thereby has to accept the proton of the Serine, hence its importance in the hydrolysis. One reaction that has recently gained considerable attention is the enzymatic degradation of polyethylene terephthalate (PET) (3–5). PET is a human-made polymer that makes up a wide variety of consumer plastics. Outstanding for its mechanical and chemical stability, these same characteristics hamper its degradation (6, 7). Plastic pollution, that can ultimately accumulate in the food chain and thereby negatively influence human health, has been recognized as a major threat to living organisms (8–10). Although members of the cutinase and lipase enzyme families had previously been identified for their capacity to degrade PET (11–14), the discovery of the *Ideonella sakaiensis* bacterium that can use PET as its sole carbon source for growth has boosted the perspectives of PET bio-remediation (15). Its PET hydrolase, named *Is*PETase, was identified, but despite extensive enzyme engineering efforts performed over the last couple of years to improve its performances (16–22), the *Is*PETase and its variants show a deterioration of their activity over a long-time reaction required to achieve 100% substrate conversion and thereby don't yet meet the requirements for a large-scale industrial application (23). Through rigorous testing of the different PETases in a standardized PET degradation assay, the thermostable Leaf-branch Compost Cutinase (LCC) enzyme (13, 24) proved to be an alternative starting candidate for optimization. Extensive mutational screening based on molecular modelling starting from the crystal structure of its inactive variant (wherein the catalytic Ser165 is mutated into an Ala residue; PDB entry 6THT.pdb) led to the LCC^{ICCG} quadruple mutant (F243I-D238C-S283C-Y127G), the first enzyme with potential in an industrial process (23, 25).

Figure 1. Catalytic triad of the LCC^{ICCG} PETase. Composed of Asp210, His242 and Ser165, the three residues are essential for the hydrolase activity. The red arrow represents schematically the attack of the Serine hydroxyl oxygen on the PET ester bond.

Because structural data of PETases with substrates remain scarce (16, 17, 26–28), we applied NMR spectroscopy to the LCC enzyme and its different variants leading to the LCC^{ICCG} mutant

(29). More recently, a similar NMR analysis of the *Fusarium solani pisi* PET-hydrolyzing cutinase (FsC) was reported (30). Whereas chemical shift perturbation (CSP) analysis upon addition of increasing amounts of a soluble substrate - mono-(2-hydroxyethyl)-terephthalate (MHET) in our case, and bis-(hydroxyethyl) terephthalate (BHET) in the FsC study - led to a molecular view of the interaction surface of the enzyme, several mechanistic aspects of the depolymerization process remain to be elucidated. One unanswered question is the reason for the alkaline pH preference for optimal activity of many of these enzymes (25, 31). Here, we address this question through a detailed heteronuclear NMR study of the histidine imidazole rings of the LCC^{ICCG} enzyme. We assign all nuclei for the 6 histidines, determine their tautomeric states as well as their pKa values, and link the latter values to the pH dependence of the degradation of both soluble and solid substrates. We thereby enhance our mechanistic understanding of the PETase reaction for this class of enzymes.

Materials and Methods

Sample preparation

[U-^{15}N]- and [U-^{13}C, ^{15}N]- labeled LCC variants have been prepared following the protocols detailed in Tournier *et al*. (25) and Charlier *et al*. (29).

The [$^{13}C^{\varepsilon 1}$-His] labeled sample preparation was adapted from Tournier *et al.* (25) and Schörghuber *et al.* (32). The gene encoding for LCC-S165A was expressed in *E. coli* BL21 (DE3) (New England Biolabs, Ipswich, MA). Proteins were overexpressed in M9 minimum media at 37 °C (42.3 mM Na_2HPO_4, 22.0 mM KH_2PO_4, 8.55 mM NaCl, 1 mM $MgSO_4$, 1 mM $CaCl_2$, 1 X Minimum Essential Medium MEM containing vitamins, 50 µg/mL kanamycin) supplemented with 1 g/L of $^{15}NH_4Cl$ with 5 g/L D-glucose. The typical volume was one liter. 20 minutes prior to induction 40 mg of [2-^{13}C]4-(2-carboxy-2-hydroxyvinyl)-*1H*-imidazolium chloride salt (the [ε_1-^{13}C] histidine precursor) was added. Protein expression was induced by adding 0.5 mM isopropyl-1-thio-β-D-galactopyranoside (IPTG) to the cell cultures followed by an overnight incubation at 21 ºC under agitation at 120 rpm. Cells were harvested by centrifugation (5000 *g*, 20 min, 4 ºC) and lysed by sonication in the presence of 0.1 mg/mL of lysozyme. Lysate was placed at 70 ºC for 30 minutes prior to centrifugation (10000*g*, 30 min, 4 ºC) and then transferred to a desalting column (HiPrep 26/10, GE Healthcare) followed by cation exchange column (HiLoad 16/10 SP Sepharose HP, GE Healthcare). Buffers for cation exchange were Buffer A = 10 mM Tp Tris pH 7.5, Buffer B = 10 mM Tp Tris pH 7.5, 1 M NaCl ; Flow rate 3 mL/min ; Elution 20% B = 150 mM NaCl. A final step of purification was performed using a size-exclusion chromatography with a a buffer containing 25 mM Tris-HCl, pH 7.5 and 100 mM NaCl on a Superdex 200 16/600 (GE Healthcare). Purity was assessed by SDS Page and by verifying the differential scanning fluorimetry (DSF) profile (25). The protein concentration was estimated by measuring the absorption at 280 nanometers using a Nanodrop (ThermoFischer, USA) and the theoretical extinction coefficient ($\varepsilon = 37150\ M^{-1}\ cm^{-1}$) estimated using the Protparam server (https://web.expasy.org/protparam). Fractions containing the pure proteins were concentrated into the same buffer.

For the pH titration series, citrate-phosphate buffer solutions in the pH range of 3 to 8 were obtained by mixing two solutions of di-sodium hydrogen phosphate dodecahydrate ($Na_2HPO_4.12H_20$, 0.5M) (≥99%) and citric acid monohydrate ($C_6H_8O_7.H_2O$, 0.5M) (≥98%) in the appropriate ratios (see Table S2). Only for the pH 9 solution, we used a phosphate buffer.

We buffer exchanged an aliquot of the enzyme under consideration to water, and concentrated the enzyme to 500µM. To a volume of 160µl of each buffer, we added 40µl of the enzyme solution, obtaining a final concentration of 100µM in each tube. The final pH in the NMR tube was verified by a ^{31}P spectrum that was simultaneously recorded with the ^{1}H 1D spectrum (33) and that was compared to the ^{31}P spectrum of the standard buffer solutions of known pH.

Crystallography

The LCC^{ICCG} variant has been prepared following the protocol detailed in Tournier *et al*. (25). Crystals were grown at 12 °C using the hanging-drop vapor diffusion method. The crystallization condition for LCC^{ICCG} (F243I/D238C/S283C/Y127G) was obtained by mixing 1 µL protein (15 mg/mL) with 1 µL reservoir buffer solution (0.1 M bicine pH 9.0, 10% PEG 20000, 2% (w/v) dioxane). A cryoprotection was performed by soaking the crystals in a solution composed of 80% mother liquor supplemented with 20% glycerol prior to data collection. Diffraction data were collected at the European Synchrotron Radiation Facility (ESRF, Grenoble, France), using the ID30-A3 beamline (MASSIF 3, wavelength 0.9677 Å). Data were processed automatically using the autoPROC toolbox (34). Molecular replacement was performed with Phaser(35) using the structure of the LCC^{ICCG}-S165A inactive enzyme (PDB code 6THT) as a search model. Refinement was conducted using PHENIX(36) and model building using Coot.(37) The final refined models contained 97.66% / 2.34%/ 0.00% in the favoured, allowed and outlier regions of the Ramachandran plot, respectively. Structural figures were prepared using the PyMOL Molecular Graphics System, version 2.3.4 (Schrödinger, LLC).

NMR section

All NMR experiments presented in this study were acquired at 30 ºC unless otherwise stated. Representative spectra and scripts are accessible on the Zenodo repository at doi : 10.5281/zenodo.10812834.

Two-dimensional ^{1}H-^{13}C HMQC experiments of U-^{13}C and His-^{13}C LCC-S165A were acquired on a Bruker AVANCE NEO 800 MHz spectrometer equipped with a 5-mm cryoprobe with z

pulsed field gradients with 8048.8 (F_1) x 11160.714 Hz (F_2) corresponding to 40 x 13.9486 ppm, with acquisition times of 15.9 ms (t_1) and 91.75 ms (t_2). RF carriers were set to 4.709 ppm (^{1}H) and 135 ppm (^{13}C). A J coupling of 210Hz was used to calculate the necessary delays in the INEPT transfer (38). Eight scans per increment were recorded. All spectra were acquired on samples containing 500 µM of protein. A representative spectrum (experiment number 2075) with pulse program and all parameters is accessible on the Zenodo repository.

The three-dimensional $^1H^N$-^{15}N-^{1}H -NOESY-TROSY experiment was recorded on a Bruker AVANCE NEO 900 MHz spectrometer equipped with CPTCI cryoprobe on a 500 µM ^{15}N-LCC^{ICCG}-S165A sample. Spectral settings for $^1H^N$-^{15}N-^{1}H-NOESY-TROSY experiment, with a mixing time of 100 ms, were 12500.022 Hz (F_1) x 2736.908 Hz (F_2) x 12500.000 Hz (F_3) corresponding to 13.8853 x 30 x 13.8853 ppm, with sampling durations of 20.48 ms (t_1), 17.5 ms (t_2), 163.8 ms (t_3). RF carriers were set to 4.7 ppm (^{1}H) and 118.5 ppm (^{15}N). Four scans per increment were recorded.

The three-dimensional $^1H^\varepsilon$-^{13}C-^{1}H -NOESY-HMQC experiment was recorded on a Bruker AVANCE NEO 800 MHz spectrometer equipped with a 5-mm cryoprobe with z pulsed field gradients on a 600µM ^{15}N/^{13}C labeled LCC^{ICCG}-S165A sample. Spectral settings for $^1H^\varepsilon$-^{13}C-^{1}H-NOESY-HMQC experiment, with a mixing time of 200 ms, were 16002.676 Hz (F_1) x 2414.643 Hz (F_2) x 11160.714 Hz (F_3) corresponding to 20 x 12 x 13.9486 ppm, with sampling durations of 19.99 ms (t_1), 9.9 ms (t_2), 91.75 ms (t_3). RF carriers were set to 4.709 ppm (^{1}H) and 136 ppm (^{13}C). Four scans per increment were recorded.

The three-dimensional best-TROSY $^1H^N$-^{15}N-^{13}C experiment (39) was recorded on a Bruker AVANCE NEO 800 MHz spectrometer equipped with a 5-mm cryoprobe with z pulsed field gradients on a 500µM ^{15}N-^{13}C-ICCG-S165A sample. Spectral settings for the best-TROSY $^1H^N$-^{15}N-^{13}C experiment, were 8051.5 Hz (F_1) x 810.898 Hz (F_2) x 16025.64 Hz (F_3) corresponding to 40 x 10 x 20.0287 ppm, with sampling durations of 31.8 ms (t_1), 19.7 ms (t_2), 63.9 ms (t_3). RF carriers were set to 4.7 ppm (^{1}H), 165 ppm (^{15}N) and 120 ppm (^{13}C). Four scans per increment were recorded. A representative spectrum (experiment number 15) with pulse program and all parameters is accessible on the Zenodo repository.

The long range ^{1}H-^{15}N HMQC spectra were recorded at 800MHz on 5mm tubes containing 300-350µM of ^{15}N/^{13}C labeled LCC^{ICCG}-S165A enzyme. The ^2J $^1H^{\varepsilon 1}$-^{15}N coupling constant was

set to 22Hz, leading to a total defocusing time in the INEPT of 22.72ms.(40) ^{13}C garp4 decoupling(41) was added during the acquisition time. The ^{15}N carrier was set to 210ppm, and the 100ppm spectral window was sampled with 164 complex points. A total of 256 scans were recorded per increment, leading to a total measurement time of 15 hours. A representative spectrum (experiment number 1075) with pulse program and all parameters is accessible on the Zenodo repository.

The $^{1}H^{\varepsilon 1}$-$^{13}C^{\varepsilon 1}$ HSQC spectra for the pH titration were recorded on 3mm samples containing 100µM of doubly labeled enzyme in the appropriate buffer. To avoid folding of other resonances, the ^{13}C carrier was set to 124ppm and the spectral window adjusted to 32ppm. Spectra were acquired as a 1k x 128 complex matrix, with 16 scans per increment.

Fitting of the pKa values : For H242 in both the LCC^{ICCG}-S165A and LCC^{ICCG}, we initially carried out a separate analysis of the proton and carbon curves using the Henderson-Hasselbalch equation with distinct pKa values for each nucleus. As this analysis lead to very similar values, we decided to fit both nuclei together to a single pKa value. We combined this analysis with a Monte Carlo approach to estimate the error bars. Python script with example dataset is accessible on the Zenodo repository. We generated 500 data sets whereby both the chemical shift and pH values were drawn from a normal distribution centered on the experimental values and with a standard deviation of 0.05 ppm for $\delta^{13}C$ and $\delta^{1}H$ chemical shift values and 0.05 units for the pH value. In Figure S6, we show the resulting distributions of the fitted pKa (blue curve), and of the low and high pH limiting values of the $\delta^{13}C$ (orange) and $\delta^{1}H$ (red) chemical shifts. The nominal values for the pKa of H242 and its error bar are given in the text and represent the mean and standard deviation of the pKa distribution.

BHET activity : Time course experiments for the hydrolysis of BHET were run with simultaneous detection of ^{1}H and ^{31}P signals in a pseudo-2D manner (33). A representative spectrum (experiment number 204/205) with pulse program and all parameters is accessible on the Zenodo repository. Starting from a saturated solution of BHET in water, 20 µL of this solution was added to 160 µL of an aqueous phosphate/citrate buffer solution at the required pH. Before adding the solution to the 3 mm NMR tube, 20 µL of D_2O and 1 mM TSP were added for locking and dosing purposes. All samples contained ~ 0.9 mM of BHET (initial concentration) and the reaction was initiated by the addition of 1 µM of the LCC^{ICCG} enzyme. This experiment was repeated 3 times, and values for the intensities of the BHET resonance are given in Table S3. Control experiments without enzyme were performed to establish BHET stability at the different pH values.

pH profile using post-consumer coloured-flake PET waste (PcW-PET)

PcW-PET was prepared according to Tournier *et al*. (25). Briefly, 9 mL of each buffer solution from the Citrate-Phosphate pH range were combined with 100 mg PcW-PET in a 40 mL round polypropylene container (Gosselin, France) and incubated at 50 °C in a Max Q 4450 incubator (Thermo Fisher Scientific, Waltham, MA) under agitation at 170 rpm until the solution reached the desired temperature. The depolymerization was initiated by adding 1 mL of a 0.05 mg_{enzyme} mL^{-1} (1.73 µM of enzyme) solution of purified protein (final concentration of 0.5 mg_{enzyme} g_{PET}^{-1}). Samples were harvested at 2, 4, and 6h of reaction time and analyzed by ultraviolet light (UV) absorbance measurements at 242 nm for the determination of PET depolymerization kinetics as described in Arnal *et al.* (23). The initial velocity (VI) of PET hydrolysis in μmol_{TPAeq} h^{-1} was determined in this linear part of the reaction. Assays were performed in triplicates.

Results

$^{1}H^{\varepsilon 1}/^{13}C^{\varepsilon 1}$ imidazole resonance assignment. We first characterized the $^{1}H^{\varepsilon 1}/^{13}C^{\varepsilon 1}$ imidazole resonances of the 6 histidines of LCC-S165A, that are expected in the [8.60-7.68] and [136.6-139.2] ppm range respectively (42). Because certain candidate peaks fell outside this range, with notably a signal at 5.84/138.6 ppm, we prepared a $^{13}C^{\varepsilon 1}$-His selectively labeled sample (32) of the inactive LCC-S165A variant to ascertain that those resonances correspond to the putative histidine imidazole signals in the uniformly doubly labeled sample. Indeed, we obtained the six expected resonances with a singlet structure in the ^{13}C dimension (Figure S1.A). When comparing the $^{1}H^{\varepsilon 1}/^{13}C^{\varepsilon 1}$ spectrum of LCC-S165A with the one from the LCC^{ICCG}-S165A, peak positions varied only slightly despite the additional mutations (Figure S1.B), and we therefore focused the rest of our study on LCC^{ICCG}.

Figure 2. Connecting the $^{1}H^{\varepsilon 1}$-$^{13}C^{\varepsilon 1}$ resonances to the H-N imidazole signals in LCC^{ICCG}-S165A. (A) HMQC spectrum with the histidine $^{1}H^{\varepsilon 1}$-$^{13}C^{\varepsilon 1}$ correlations. **(B)** Magnetization flow in the original (39) (orange) and the modified (blue) pulse sequence. Both τ and π tautomers are shown for clarity. **(C)** Overlay of the 2D $^{1}H^{N}$-^{13}C planes extracted at the $^{15}N^{\varepsilon 2}$ frequency of H112, H164, H191 and H291 (dark blue) and the $N^{\delta 1}$ frequency of H242 (light blue). The inserts show the line shape in the ^{13}C dimension, with a singlet for all $^{13}C^{\varepsilon 1}$ nuclei, a doublet for the $^{13}C^{\delta 2}$ signals of the four τ tautomers and a triplet for the $^{13}C^{\gamma}$ of H242. **(D)** Overlay of (red) a $^{1}H^{N}$-^{15}N TROSY spectrum acquired with 16 scans and (grey) a best-TROSY (43) spectrum acquired with 128 scans.

Assignment of the six identified resonances was carried out using NOESY-based experiments that were interpreted with the help of the crystal structure of LCC^{ICCG}-S165A (PDB code 6THT) (25). The crystal structure was used to identify nearest neighbor residues for the $^{1}H^{\varepsilon 1}$ proton of each imidazole ring (Figure S2.A & B). Extracting the 2D $^{1}H^{N}$-^{1}H strip from a $^{1}H^{N}$-^{15}N-^{1}H NOESY-TROSY experiment at the amide nitrogen frequency of these proximal residues and comparing with the six 2D $^{1}H^{\varepsilon 1}$-^{1}H strips extracted from a $^{1}H^{\varepsilon 1}$-$^{13}C^{\varepsilon 1}$-^{1}H NOESY-HMQC centered on each $^{13}C^{\varepsilon 1}$ frequency led to the assignment of all imidazole $^{1}H^{\varepsilon 1}/^{13}C^{\varepsilon 1}$ resonances (Figures 2.A & S2.C).

Imidazole nitrogens and tautomeric states. Histidine residues equally contain one or two nitrogen bonded proton(s) on their imidazole ring (on $N^{\delta1}$ and/or $N^{\varepsilon2}$, according to the tautomer and charge state) (Figure 2.B). In a large window ^{1}H-^{15}N correlation spectrum, we observed 5 rather than 6 correlation peaks with ^{15}N chemical shift around 165 ppm and proton chemical shift varying from 10 to 14 ppm (Figure 2.D, Figure S3). We initially sought to assign these $^{1}H^{N}$-^{15}N imidazole signals by transferring the magnetization from the $^{1}H^{N\varepsilon2}$ via the $^{13}C^{\delta}$ and $^{13}C^{\gamma}$ carbons (39) to the previously assigned (29) $^{13}C^{\beta}$ signal (Figure 2.B, orange arrows). However, magnetization transfer beyond the $^{13}C^{\gamma}$ proved inefficient, likely due to the size of the protein (28 kDa). Therefore, we modified the pulse sequence (Figure S4) to allow magnetization flow from the $^{1}H^{N}$-^{15}N cross peaks to the neighboring carbons, including the previously assigned $^{13}C^{\varepsilon1}$ frequency (Figure 2.B, blue arrows). When extracting the $^{1}H^{N}$-^{13}C plane for these 5 peaks with ^{15}N chemical shift around 165 ppm, we observed at the ^{15}N frequency of four of them both a singlet and a doublet in the ^{13}C dimension (Figure 2.C). The singlet corresponds to the imidazole $^{13}C^{\varepsilon1}$ carbon between both nitrogens and could be connected to the assigned $^{1}H^{\varepsilon1}/^{13}C^{\varepsilon1}$ spectrum (Figure 2.A), whereas the doublet represents the $^{13}C^{\delta2}$ carbon with a single coupling constant towards its $^{13}C^{\gamma}$ neighbor (Figure 2.C, blue inset). The latter doublet structure and their $^{13}C^{\delta2}$ chemical shift value below 122 ppm (44) confirm the τ tautomer for those 4 histidines.

For the most downfield shifted $^{1}H^{N}$ peak at 13.9 ppm, magnetization transfer in the triple resonance HCN experiment also led to a singlet, but the other peak is a triplet rather than a doublet (Figure 2.C, light blue insert). This triplet structure is assigned to a His $^{13}C^{\gamma}$ with couplings to its $^{13}C^{\delta2}$ and $^{13}C^{\beta}$ nuclei as expected for an imidazole ring in the π tautomeric state. We assigned it unambiguously to the catalytic H242 with the previously described $^{1}H^{\varepsilon1}$-$^{13}C^{\varepsilon1}$-^{1}H NOESY-HMQC experiment, where the obligatory short distance (2.4 Å) between the $H^{\varepsilon1}$ and the nitrogen linked proton indeed showed up as a strong NOE contact (Figure S5). While the same approach confirmed the other previously assigned imidazole resonances, we did not observe any NOE cross peak for H218. This is most probably a sensitivity issue, as its $H^{\varepsilon2}/N^{\varepsilon2}$ resonance was already much broader in the 2D spectrum and required an extended acquisition time to be observable (Figure 2.D, grey spectrum).

The tautomeric state of the histidine rings can also be deduced from the $^{2}J_{NH}$ $^{1}H^{\varepsilon1}$-^{15}N scalar coupling pattern in a long range ^{1}H-^{15}N HMQC spectrum (40). For the τ tautomers, we expect a strong cross peak from the $^{1}H^{\varepsilon1}$ to the $^{15}N^{\delta1}$ in the 240/260 ppm range and a weaker correlation

at $^{1}H^{\varepsilon1}/^{15}N^{\varepsilon2}$ with the latter nucleus resonating in the range of 160/170 ppm (40). We observed such pattern for 5 out of 6 histidines, and could thereby assign the τ tautomer to the missing H218 resonance (Figure 3). For H242, we observed a different pattern, with two peaks at the same ^{15}N frequency of 247.5 ppm. This is the expected pattern for an imidazole ring in the π tautomeric state, where the $^{15}N^{\varepsilon2}$ nitrogen with its lone orbital is within $^{2}J_{NH}$ distance of both the $^{1}H^{\varepsilon1}$ and $^{1}H^{\delta2}$ protons (Figure 3, insert).

Figure 3. Identification of the tautomeric state of the histidines in LCC^{ICCG}-S165A using long range scalar couplings. (A) $^{1}H^{\varepsilon1}$-^{15}N HMQC spectrum showing the signals of protonated (160-176 ppm, top part of the panel) and non-protonated (240-260 ppm, bottom part of the panel) ^{15}N nuclei. For imidazole rings in the τ tautomeric state such as H218, we observe a strong $H^{\varepsilon1}/N^{\delta1}$ and a weaker $H^{\varepsilon1}/N^{\varepsilon2}$ correlation (connected by a blue line). For H242 in the π tautomer state (red line), both $^{1}H^{\varepsilon1}$ and $^{1}H^{\delta2}$ protons connect to the $^{15}N^{\varepsilon2}$ resonance (insert, red arrows), whereas only the $H^{\varepsilon1}$ connects to the protonated $N^{\delta1}$ (insert, green arrow). **(B)** Assigned $^{1}H^{\varepsilon1}$-$^{13}C^{\varepsilon1}$ HMQC spectrum.

Determining the imidazole pKa values. The notion of τ or π tautomeric form disappears when the imidazole rings become doubly protonated at pH values below their pKa. Protonation of the imidazole nitrogen ($N^{\delta1}/N^{\varepsilon2}$ for the τ/π tautomer) has a dramatic effect on its chemical shift, with variations as large as 80ppm expected (from 250-240 to 170-160 ppm) (45–47), and should hence form the ideal probe to determine its pKa. A series of ^{2}J long-range $^{1}H^{\varepsilon1}$-^{15}N HMQC spectra was recorded while varying the pH from 4.0 to 9.0 (Figure 4.A). Importantly, four peaks (belonging to H218, H191, H291 and H112) hardly move over this pH range; their $^{15}N^{\delta1}$ nitrogen frequency remains around 250 ppm for all pH values and only at pH 4 do we observe the first shifts (Figure 4.A, insert). This excludes their protonation and unambiguously indicates that all four have a pKa value lower than 4. For H242, the $N^{\varepsilon2}$ frequency as seen from both correlations to its $H^{\varepsilon1}$ and $H^{\delta2}$ protons starts shifting earlier, with a visible peak shift already present at pH 7.5, and with 4.3 and 10.6 ppm variations in the nitrogen dimension at pH 6.0 and 5.5 respectively (Figure 4.A). However, both their weakening intensity with decreasing pH and their nitrogen chemical shifts approaching those of the folded amide peaks (Figure S6) prevented us from following this peak over the full pH range and hence establish a reliable titration curve. We thus exploited the assigned $^{1}H^{\varepsilon1}$-$^{13}C^{\varepsilon1}$ signals as an alternative probe for the

protonation of the individual imidazole rings. For the catalytic histidine, H242, this $^{1}H^{\varepsilon 1}$-$^{13}C^{\varepsilon 1}$ peak significantly shifted in both ^{1}H and ^{13}C dimensions when varying the pH (Figure 4.B). Both profiles as a function of pH were fitted to the Henderson-Hasselbalch equation and yielded the same pKa value of 4.79±0.04 (Figure 4.C). Whereas no shifts were observed for the same $^{1}H^{\varepsilon 1}$-$^{13}C^{\varepsilon 1}$ correlation of the H218, H191, H291 and H112 imidazole rings, in agreement with their previously mentioned invariant $^{15}N^{\delta 1}$ frequencies, H164 displayed a small displacement in the proton dimension only. However, its constant $^{13}C^{\varepsilon 1}$ chemical shift and the downfield shift of its $N^{\delta 1}$ resonance upon decreasing pH (Figure 4.A, insert) indicate that the peak displacement in the pH 4-8 range is most probably not dominated by its own protonation state. Protonation of the nearby H242 ring is a good candidate, and when the ^{1}H curve of H164 was fitted to a Henderson-Hasselbalch equation with a pKa value of 4.79 as determined for H242, we obtained a very good agreement (Figure S7).

Fig. 4. pH titration of the different imidazole $H^{\varepsilon 1}$-$C^{\varepsilon 1}$ resonances in LCC^{ICCG}-S165A. **(A)** Long-range $^{1}H^{\varepsilon 1}$-^{15}N spectra showing the expected upfield shift that accompanies protonation of H242. (insert) For the cross peaks characterizing the imidazole rings of H112 and H191, we start observing an upfield shift when the pH reaches 4.5. The resonance of H164, on the contrary, shifts downfield upon decreasing the pH, which cannot correspond to an increase in its own protonation level. **(B)** $^{1}H^{\varepsilon 1}$-$^{13}C^{\varepsilon 1}$ HMQC spectra acquired as a function of pH. Only the resonance of the catalytic H242 shifts appreciably in both dimensions. **(C)** $^{1}H^{\varepsilon 1}$ (blue) and $^{13}C^{\varepsilon 1}$ (red) chemical shift values of the catalytic histidine (H242) plotted as a function of pH. The dots represent experimental data whereas the solid lines correspond to the best fit to the Henderson-Hasselbalch equation leading to a single pKa value of 4.79 ± 0.04. For a statistical analysis of the curve fit, see Figure S8 in the SI.

Linking pKa and pH profile of the hydrolase activity. All data presented until here were obtained using the inactive LCC^{ICCG}-S165A variant, mostly because of its very high expression level and the capacity to study interactions with small substrates without hydrolysis. However, to probe the relationship between activity and the determined pKa values requires an active enzyme. We thus doubled the volume of the bacterial culture, obtained a $^{13}C/^{15}N$ labeled sample

of the active LCC^{ICCG} enzyme and repeated the histidine targeting NMR experiments. We simultaneously solved the crystal structure of the active enzyme. The Cα-RMSD between both structures (active LCC^{ICCG}: PDB code 8OTA ; inactive LCC^{ICCG}-S165A: PDB code 6THT) was limited to 0.15Å, and the active site was particularly well conserved (Figure 5.A). Despite this near-identical structure, the chemical shift of the H242 $^{1}H^{\varepsilon 1}$-$^{13}C^{\varepsilon 1}$ correlation differs significantly between both proteins (Figure 5.B). Evidently, the methyl group of A165 is replaced by a S165 hydroxyl group in the active variant, and this moiety directly faces the H242 imidazole ring, which can explain the chemical shift difference. The resonances of H164 and to a lesser extent of H218, with distances of 5.5Å and 8.1Å, respectively, between their $H^{\varepsilon 1}$ proton and the hydroxyl oxygen of S165, also have their $^{1}H^{\varepsilon 1}/^{13}C^{\varepsilon 1}$ resonances impacted.
When repeating the pH titration experiment with the $^{1}H^{\varepsilon 1}/^{13}C^{\varepsilon 1}$ peak as read-out (Figure S9.A), we found a value of 4.90 ± 0.05 for the pKa of the catalytic H242 in the active enzyme (Figure 6.A & B), slightly higher than the value found for the inactive variant. Broadening of the $^{1}H^{\varepsilon 1}/^{13}C^{\varepsilon 1}$ peaks in the spectra around this pKa value was more pronounced in the active variant (compare Figures 4.B and 6.A), suggesting that the presence of a Serine hydroxyl proton next to the imidazole $N^{\varepsilon 2}$ (Figure 1) changes the dynamics of its (de)protonation. None of the other imidazole resonances shifted appreciably over this pH range (Figure S9.A), indicating that their pKa values remain below 4.

Fig. 5. Comparison of the inactive S165A (blue) and active S165 (red) LCC^{ICCG} enzymes. **(A)** Structural comparison of the catalytic triads in the crystal structures of both enzymes. **(B)** $^{1}H^{\varepsilon 1}$-$^{13}C^{\varepsilon 1}$ spectra of both enzymes showing the downfield shift of the H242 cross peak in the active enzyme.

To evaluate the importance of these pKa values for the catalytic process, we first monitored the hydrolysis of BHET by the active LCC^{ICCG} enzyme as a function of pH. The degenerate aromatic signal of BHET was found to decrease over time (Figure S10.A). Time course curves of the BHET signal intensity during this reaction at pH values ranging from 4 to 8 (Figure S10.B) were fitted to obtain the pH dependence of the rate of hydrolysis. The optimum pH is in the range of 6 to 8 with significant activity remaining over the whole pH range (67.5, 32.5 and 15% at pH 5, 4.5 and 4, respectively) (Figure 6.C). When plotting the protonation state of

the catalytic histidine on this graph using the experimentally determined pKa value of 4.90, we observe good agreement, suggesting that the protonation state of H242 can satisfactorily explain the activity profile as a function of pH.

Because previous studies with lipases and/or cutinases hinted at different pH dependence of the activity towards soluble or insoluble substrates (48), we also set up an experiment to follow the degradation of PET powder in a pH dependent manner. This experiment requires a higher temperature than the BHET hydrolysis (50°C in our experiment) (23), so we first measured the pKa of the catalytic histidine H242 at this temperature. When fitting the chemical shifts in the spectra between pH 8.0 and pH 4.0, we obtained a value of 4.70 ± 0.04 for the pKa of the catalytic H242 at 50 °C (Figure 6.B and S11), slightly lower as expected than its value at 30 °C (49).

Fig. 6. LCC^{ICCG} catalyzed hydrolysis of soluble and insoluble species as a function of pH. **(A)** Zoom on the H242 $^{1}H^{\varepsilon 1}$-$^{13}C^{\varepsilon 1}$ resonance at 30ºC as a function of pH. **(B)** H242 $^{1}H^{\varepsilon 1}$ and $^{13}C^{\varepsilon 1}$ chemical shift values as a function of pH. The dots represent the experimental data. The best fit towards the Henderson-Hasselbalch equation (line) gives a pKa value of 4.90 ± 0.05. **(C)** pH dependent rates of hydrolysis of BHET. Circles and triangles represent experimental data points of two independent series. The dashed line corresponds to the H242 protonation state based on the Henderson-Hasselbalch equation with the pKa fixed to the experimentally determined value of 4.90. (D) Zoom on the H242 $^{1}H^{\varepsilon 1}$-$^{13}C^{\varepsilon 1}$ resonance at 50ºC as function of pH. (E) $^{1}H^{\varepsilon 1}$ and $^{13}C^{\varepsilon 1}$ chemical shift curves of H242 as a function of pH at 50ºC. The dots represent the experimental values and the line displays the best fit towards the Henderson-Hasselbalch equation, yielding a pKa value of 4.70 ± 0.05. (F) Hydrolysis of PET powder as function of pH. Dots represent experimental initial velocities as a function of pH, whereas the protonation/deprotonation curve of H242 at 50 °C is modeled as a dashed line with a pKa value of 4.70.

In the PET powder degradation experiment, the initial velocities cannot be modeled satisfactorily with the above determined pKa value of 4.70, as we observe a steep pH

dependence with a drop to half of the optimal efficacy at pH 8.0 already obtained at a pH value of 6.5 (Figure 6.F). For the triolein film degradation by FsC, a similar steeper pH dependence than that predicted by the pKa value of its catalytic histidine was previously described (48). However, whereas in this latter study, a sizeable activity remained even at pH values inferior by 1.5 units to the pKa of its catalytic H188, we found little to no catalytic activity of the LCC^{ICCG} cutinase on the PET powder once below the pKa value of its catalytic H242.

Discussion

Serine proteases act mostly at neutral to slightly alkaline conditions (50). Different molecular models for their activity include the charge-relay model (51) or a reaction-driven histidine ring flip mechanism (52), but all require a neutral catalytic histidine in the resting state that can accept the proton of the catalytic serine hydroxyl (Figure 1) (2, 46, 53). PETases, as part of the larger family of serine hydrolases, equally function at an optimal pH value near or above 8, independently of whether they are isolated from natural organisms or further improved by different engineering strategies (13, 15, 21, 25).

In order to better understand this pH dependence, we have characterized in the present study the histidine residues of LCC^{ICCG}, an optimized PETase (25). Based on the assignment of the different nuclei of the six imidazole rings (Figure 2), we confirm the τ tautomer for all Histidines except the catalytic H242 (Figure 3). The π tautomeric state for the catalytic histidine has been observed for all serine proteases acting on amide bonds (46, 54), and our analysis shows that the LCC^{ICCG} PETase, with its activity towards ester bonds, is no exception.
Using the $H^{\varepsilon 1}/C^{\varepsilon 1}$ resonances of the imidazole rings directly as a probe and not the chemical shift values of the surrounding amide moieties that can combine the information of different charge groups and thereby can yield an erroneous estimate (48, 55), we obtain a value of 4.79 for the pKa of H242 in the inactive LCC^{ICCG}-S165A enzyme (Figure 4) and values of 4.90 or 4.70 for the active enzyme at 30 °C and 50 °C, respectively (Figure 6). Already significantly lower than the usual value of 6.5 for histidines in proteins, all 5 other histidines are characterized by even lower pKa values with no visible shifts of their $N^{\delta 1}$ resonance above pH 4.0 (Figure 4.A). Values below 2.3 have been reported for H24 in a folding intermediate of apomyoglobulin (56), and values of 2.8 were measured for selected histidines in the immunophilins Cyclophilin A and FKBP, where they were attributed to the positively charged surroundings (57). A charged environment could also be invoked for H218 in LCC^{ICCG}, which directly faces the ammonium

group of the K194 side chain, for H291 surrounded by R290 and R271 or for H112 with R108 (Figure S12). H191, in contrast, has no obvious positive charges in its direct environment, but burial of its imidazole group could influence its low pKa value (58).

Previous work with FsC had shown a good agreement between the pKa value of 5 obtained for its catalytic H188 and its activity profile against a soluble substrate (48). The good concordance that we find between the hydrolytic activity curve of LCC^{ICCG} against BHET as a function of pH and the protonation state of its H242 (Figure 6.C) underscores the functional relevance of our NMR analysis of the histidines of LCC^{ICCG}. However, and in contrast with previous findings that BHET degradation was suitable to estimate enzymatic surface hydrolysis of PET (59), the activity curve as a function of pH with an insoluble substrate (here, PET powder) could not be modeled by the same pKa value (Figure 6.F). This finding confirms the similar discrepancy that was observed for the pH dependence of FsC degrading a triolein film (48). Surface acidification resulting from carboxylic acids formed upon ester bond cleavage could lead to a substantial lowering of pH at the polymer surface, both for the PET and for triolein solid surfaces. Such polymer surface acidification could directly affect the protonation state of the catalytic histidine and provide an explanation for the loss of enzymatic activityat pH 6.5, which is almost two units above its determined pKa. The solid PET substrate depolymerization efficiency could also depend on surface adsorption and desorption of the enzyme. These latter processes, with a high affinity (60) and low off-rate (61) for LCC^{ICCG}, could be influenced by pH.

In conclusion, we provide an extensive characterization of the different histidines of the improved LCC^{ICCG} PETase. We show that all imidazole rings are in the τ tautomer, except for the catalytic H242 in the π tautomer. The presence of the catalytic Ser165 rather than an Ala165 in the inactive form does not influence the structure of the enzyme or of its active site, although it affects selected resonances in a distinct manner. The pKa values for all histidines were below 4, with the exception of H242 for which we determined a pKa value of 4.90 at 30 °C and 4.70 at 50 °C in its active form. Whereas this pKa value allows satisfactory modeling of the pH dependent hydrolysis of BHET as a soluble substrate, the pH dependent activity curve with PET powder deviates in an important manner from the same model. Values of local pH influenced by the generation of acidic functions during the degradation process hence have to be considered.

Author Contributions

CC and GL conceived the project. CC, SG, JG, LP, VG, and GL performed experiments. CC, SG, GA, AM, VT and GL analyzed data. FL, JS and RL contributed materials. CC, AM, VT and GL wrote the manuscript, that was approved by all authors.

Acknowledgments

We thank the ICEO facility of the Toulouse Biotechnology Institute (TBI), which is part of the Integrated Screening Platform of Toulouse (PICT, IBiSA), for providing access to protein-purification equipment. We thank the NMR facility of MetaToul (Toulouse metabolomics & fluxomics facilities, www.metatoul.fr). Metatoul is part of the French National Infrastructure for Metabolomics and Fluxomics MetaboHUB-AR-11-INBS-0010 (www.metabohub.fr), and is supported by the Région Midi-Pyrénées, the ERDF, the SICOVAL and the French Minister of Education & Research, who are all gratefully acknowledged. We thank Dr FX Cantrelle for expert help with the 900MHz NMR instrument in Lille. Financial support from the IR-RMN-THC Fr3050 CNRS for conducting the research is gratefully acknowledged. We thank Dr C Byrne (Cergy Paris University) for careful proofreading of the final version.

This study was supported by Carbios and a grant-in-aid for scientific research (Circular Economy PET project financed by ADEME - contract number 1882C0098).

Declaration of interest S.G., L.P., G.A., A.M., and V.T. are employees of Carbios and confidentiality agreements prevent them from disclosing any newly submitted declaration of invention. A.M., and V.T. have filed patents WO 2018/011284, WO 2018/011281, and WO 2020/021118 entitled “Novel esterases and uses thereof”. All other authors declare no competing interests.

Figure Legends

Figure 1. Catalytic triad of the LCC^{ICCG} PETase. Composed of Asp210, His242 and Ser165, the three residues are essential for the hydrolase activity. The red arrow represents schematically the attack of the Serine hydroxyl oxygen on the PET ester bond.

Figure 2. Connecting the $^{1}H^{\varepsilon 1}$-$^{13}C^{\varepsilon 1}$ resonances to the H-N imidazole signals in LCC^{ICCG}-S165A. (A) HMQC spectrum with the histidine $^{1}H^{\varepsilon 1}$-$^{13}C^{\varepsilon 1}$ correlations. **(B)** Magnetization flow in the original (39) (orange) and the modified (blue) pulse sequence. Both τ and π tautomers are shown for clarity. **(C)** Overlay of the 2D $^{1}H^{N}$-^{13}C planes extracted at the $^{15}N^{\varepsilon 2}$ frequency of H112, H164, H191 and H291 (dark blue) and the $N^{\delta 1}$ frequency of H242 (light blue). The inserts show the line shape in the ^{13}C dimension, with a singlet for all $^{13}C^{\varepsilon 1}$ nuclei, a doublet for the $^{13}C^{\delta 2}$ signals of the four τ tautomers and a triplet for the $^{13}C^{\gamma}$ of H242. **(D)** Overlay of (red) a $^{1}H^{N}$-^{15}N TROSY spectrum acquired with 16 scans and (grey) a best-TROSY (43) spectrum acquired with 128 scans.

Figure 3. Identification of the tautomeric state of the histidines in LCC^{ICCG}-S165A using long range scalar couplings. (A) $^{1}H^{\varepsilon 1}$-^{15}N HMQC spectrum showing the signals of protonated (160-176 ppm, top part of the panel) and non-protonated (240-260 ppm, bottom part of the panel) ^{15}N nuclei. For imidazole rings in the τ tautomeric state such as H218, we observe a strong $H^{\varepsilon 1}/N^{\delta 1}$ and a weaker $H^{\varepsilon 1}/N^{\varepsilon 2}$ correlation (connected by a blue line). For H242 in the π tautomer state (red line), both $^{1}H^{\varepsilon 1}$ and $^{1}H^{\delta 2}$ protons connect to the $^{15}N^{\varepsilon 2}$ resonance (insert, red arrows), whereas only the $H^{\varepsilon 1}$ connects to the protonated $N^{\delta 1}$ (insert, green arrow). **(B)** Assigned $^{1}H^{\varepsilon 1}$-$^{13}C^{\varepsilon 1}$ HMQC spectrum.

Figure 4. pH titration of the different imidazole $H^{\varepsilon 1}$-$C^{\varepsilon 1}$ resonances in LCC^{ICCG}-S165A. **(A)** Long-range $^{1}H^{\varepsilon 1}$-^{15}N spectra showing the expected upfield shift that accompanies protonation of H242. (insert) For the cross peaks characterizing the imidazole rings of H112 and H191, we start observing an upfield shift when the pH reaches 4.5. The resonance of H164, on the contrary, shifts downfield upon decreasing the pH, which cannot correspond to an increase in its own protonation level. **(B)** $^{1}H^{\varepsilon 1}$-$^{13}C^{\varepsilon 1}$ HMQC spectra acquired as a function of pH. Only the resonance of the catalytic H242 shifts appreciably in both dimensions. **(C)** $^{1}H^{\varepsilon 1}$

(blue) and $^{13}C^{\varepsilon 1}$ (red) chemical shift values of the catalytic histidine (H242) plotted as a function of pH. The dots represent experimental data whereas the solid lines correspond to the best fit to the Henderson-Hasselbalch equation leading to a single pKa value of 4.79 ± 0.04. For a statistical analysis of the curve fit, see Figure S8 in the SI.

Figure 5. Comparison of the inactive S165A (blue) and active S165 (red) LCC^{ICCG} enzymes. (A) Structural comparison of the catalytic triads in the crystal structures of both enzymes. **(B)** $^{1}H^{\varepsilon 1}$-$^{13}C^{\varepsilon 1}$ spectra of both enzymes showing the downfield shift of the H242 cross peak in the active enzyme.

Figure 6. LCC^{ICCG} catalyzed hydrolysis of soluble and insoluble species as a function of pH. (A) Zoom on the H242 $^{1}H^{\varepsilon 1}$-$^{13}C^{\varepsilon 1}$ resonance at 30ºC as a function of pH. **(B)** H242 $^{1}H^{\varepsilon 1}$ and $^{13}C^{\varepsilon 1}$ chemical shift values as a function of pH. The dots represent the experimental data. The best fit towards the Henderson-Hasselbalch equation (line) gives a pKa value of 4.90 ± 0.05. **(C)** pH dependent rates of hydrolysis of BHET. Circles and triangles represent experimental data points of two independent series. The dashed line corresponds to the H242 protonation state based on the Henderson-Hasselbalch equation with the pKa fixed to the experimentally determined value of 4.90. (D) Zoom on the H242 $^{1}H^{\varepsilon 1}$-$^{13}C^{\varepsilon 1}$ resonance at 50ºC as function of pH. (E) $^{1}H^{\varepsilon 1}$ and $^{13}C^{\varepsilon 1}$ chemical shift curves of H242 as a function of pH at 50ºC. The dots represent the experimental values and the line displays the best fit towards the Henderson-Hasselbalch equation, yielding a pKa value of 4.70 ± 0.05. (F) Hydrolysis of PET powder as function of pH. Dots represent experimental initial velocities as a function of pH, whereas the protonation/deprotonation curve of H242 at 50 °C is modeled as a dashed line with a pKa value of 4.70.

References

1. Rauwerdink, A., and R.J. Kazlauskas. 2015. How the Same Core Catalytic Machinery Catalyzes 17 Different Reactions: the Serine-Histidine-Aspartate Catalytic Triad of α/β-Hydrolase Fold Enzymes. *ACS Catal.* 5:6153–6176.

2. Steitz, T.A., and R.G. Shulman. 1982. Crystallographic and NMR Studies of the Serine Proteases. *Annu. Rev. Biophys. Bioeng.* 11:419–444.

3. Kawai, F. 2021. The Current State of Research on PET Hydrolyzing Enzymes Available for Biorecycling. *Catalysts*. 11:206.

4. Tournier, V., S. Duquesne, F. Guillamot, H. Cramail, D. Taton, A. Marty, and I. André. 2023. Enzymes' Power for Plastics Degradation. *Chem. Rev.*

5. Mican, J., D. 'san M.M. Jaradat, W. Liu, G. Weber, S. Mazurenko, U.T. Bornscheuer, J. Damborsky, R. Wei, and D. Bednar. 2024. Exploring new galaxies: Perspectives on the discovery of novel PET-degrading enzymes. *Appl. Catal. B-Environ. ENERGY*. 342:123404.

6. Chamas, A., H. Moon, J. Zheng, Y. Qiu, T. Tabassum, J.H. Jang, M. Abu-Omar, S.L. Scott, and S. Suh. 2020. Degradation Rates of Plastics in the Environment. *ACS Sustain. Chem. Eng.* 8:3494–3511.

7. Iroegbu, A.O.C., S.S. Ray, V. Mbarane, J.C. Bordado, and J.P. Sardinha. 2021. Plastic Pollution: A Perspective on Matters Arising: Challenges and Opportunities. *ACS Omega*. 6:19343–19355.

8. Lehel, J., and S. Murphy. 2021. Microplastics in the Food Chain: Food Safety and Environmental Aspects. *Rev. Environ. Contam. Toxicol.* 259:1–49.

9. Cverenkárová, K., M. Valachovičová, T. Mackuľak, L. Žemlička, and L. Bírošová. 2021. Microplastics in the Food Chain. *Life*. 11:1349.

10. Abdolahpur Monikh, F., S. Holm, R. Kortet, M. Bandekar, J. Kekäläinen, A. Koistinen, J.T.T. Leskinen, J. Akkanen, H. Huuskonen, A. Valtonen, L. Dupuis, W. Peijnenburg, I. Lynch, E. Valsami-Jones, and J.V.K. Kukkonen. 2022. Quantifying the trophic transfer of sub-micron plastics in an assembled food chain. *Nano Today*. 46:101611.

11. Tokiwa, Y., and T. Suzuki. 1977. Hydrolysis of polyesters by lipases. *Nature*. 270:76–78.

12. Kengo, K., T. Uschara, N. Ryota, N. Kousuke, K. Hajime, S. Hideyuki, and K. Fusako. 2012. Crystal structure of cutinase Est119 from Thermobifida alba AHK119 that can degrade modified polyethylene terephthalate at 1.76Å resolution. *Polym. Degrad. Stab.* 97:771–775.

13. Sulaiman, S., S. Yamato, E. Kanaya, J.-J. Kim, Y. Koga, K. Takano, and S. Kanaya. 2012. Isolation of a Novel Cutinase Homolog with Polyethylene Terephthalate-Degrading Activity from Leaf-Branch Compost by Using a Metagenomic Approach. *Appl. Environ. Microbiol.* 78:1556–1562.

14. Sui, B., T. Wang, J. Fang, Z. Hou, T. Shu, Z. Lu, F. Liu, and Y. Zhu. 2023. Recent advances in the biodegradation of polyethylene terephthalate with cutinase-like enzymes. *Front. Microbiol.* 14:1265139.

15. Yoshida, S., K. Hiraga, T. Takehana, I. Taniguchi, H. Yamaji, Y. Maeda, K. Toyohara, K. Miyamoto, Y. Kimura, and K. Oda. 2016. A bacterium that degrades and assimilates poly(ethylene terephthalate). *Science*. 351:1196–1199.

16. Han, X., W. Liu, J.-W. Huang, J. Ma, Y. Zheng, T.-P. Ko, L. Xu, Y.-S. Cheng, C.-C. Chen, and R.-T. Guo. 2017. Structural insight into catalytic mechanism of PET hydrolase. *Nat. Commun.* 8.

17. Joo, S., I.J. Cho, H. Seo, H.F. Son, H.-Y. Sagong, T.J. Shin, S.Y. Choi, S.Y. Lee, and K.-J. Kim. 2018. Structural insight into molecular mechanism of poly(ethylene terephthalate) degradation. *Nat. Commun.* 9.

18. Austin, H.P., M.D. Allen, B.S. Donohoe, N.A. Rorrer, F.L. Kearns, R.L. Silveira, B.C. Pollard, G. Dominick, R. Duman, K. El Omari, V. Mykhaylyk, A. Wagner, W.E. Michener, A. Amore, M.S. Skaf, M.F. Crowley, A.W. Thorne, C.W. Johnson, H.L. Woodcock, J.E. McGeehan, and G.T. Beckham. 2018. Characterization and engineering of a plastic-degrading aromatic polyesterase. *Proc. Natl. Acad. Sci. U. S. A.* 115:E4350–E4357.

19. Son, H.F., I.J. Cho, S. Joo, H. Seo, H.-Y. Sagong, S.Y. Choi, S.Y. Lee, and K.-J. Kim. 2019. Rational Protein Engineering of Thermo-Stable PETase from *Ideonella sakaiensis* for Highly Efficient PET Degradation. *ACS Catal.* 9:3519–3526.

20. Bell, E.L., R. Smithson, S. Kilbride, J. Foster, F.J. Hardy, S. Ramachandran, A.A. Tedstone, S.J. Haigh, A.A. Garforth, P.J.R. Day, C. Levy, M.P. Shaver, and A.P. Green. 2022. Directed evolution of an efficient and thermostable PET depolymerase. *Nat. Catal.* 5:673–681.

21. Lu, H., D.J. Diaz, N.J. Czarnecki, C. Zhu, W. Kim, R. Shroff, D.J. Acosta, B.R. Alexander, H.O. Cole, Y. Zhang, N.A. Lynd, A.D. Ellington, and H.S. Alper. 2022. Machine learning-aided engineering of hydrolases for PET depolymerization. *Nature*. 604:662–667.

22. Soong, Y.V., U. Abid, A.C. Chang, C. Ayafor, A. Patel, J. Qin, J. Xu, C. Lawton, H. Wong, M.J. Sobkowicz, and D. Xie. 2023. Enzyme selection, optimization, and production toward biodegradation of post-consumer poly(ethylene terephthalate) at scale. *Biotechnol. J.* 18:2300119.

23. Arnal, G., J. Anglade, S. Gavalda, V. Tournier, N. Chabot, U.T. Bornscheuer, G. Weber, and A. Marty. 2023. Assessment of Four Engineered PET Degrading Enzymes Considering Large-Scale Industrial Applications. *ACS Catal.* 13:13156–13166.

24. Sulaiman, S., D.-J. You, E. Kanaya, Y. Koga, and S. Kanaya. 2014. Crystal Structure and Thermodynamic and Kinetic Stability of Metagenome-Derived LC-Cutinase. *Biochemistry*. 53:1858–1869.

25. Tournier, V., C.M. Topham, A. Gilles, B. David, C. Folgoas, E. Moya-Leclair, E. Kamionka, M.-L. Desrousseaux, H. Texier, S. Gavalda, M. Cot, E. Guémard, M. Dalibey, J. Nomme, G. Cioci, S. Barbe, M. Chateau, I. André, S. Duquesne, and A. Marty. 2020. An engineered PET depolymerase to break down and recycle plastic bottles. *Nature*. 580:216–219.

26. Richter, P.K., P. Blázquez-Sánchez, Z. Zhao, F. Engelberger, C. Wiebeler, G. Künze, R. Frank, D. Krinke, E. Frezzotti, Y. Lihanova, P. Falkenstein, J. Matysik, W. Zimmermann, N. Sträter, and C. Sonnendecker. 2023. Structure and function of the metagenomic plastic-degrading polyester hydrolase PHL7 bound to its product. *Nat. Commun.* 14:1905.

27. Yang, Y., S. Cheng, Y. Zheng, T. Xue, J.-W. Huang, L. Zhang, Y. Yang, R.-T. Guo, and C.-C. Chen. 2024. Remodeling the polymer-binding cavity to improve the efficacy of PBAT-degrading enzyme. *J. Hazard. Mater.* 464:132965.

28. Zeng, W., X. Li, Y. Yang, J. Min, J.-W. Huang, W. Liu, D. Niu, X. Yang, X. Han, L. Zhang, L. Dai, C.-C. Chen, and R.-T. Guo. 2022. Substrate-Binding Mode of a Thermophilic PET Hydrolase and Engineering the Enzyme to Enhance the Hydrolytic Efficacy. *ACS Catal.* 12:3033–3040.

29. Charlier, C., S. Gavalda, V. Borsenberger, S. Duquesne, A. Marty, V. Tournier, and G. Lippens. 2022. An NMR look at an engineered PET depolymerase. *Biophys. J.* 121:2882–2894.

30. Hellesnes, K.N., S. Vijayaraj, P. Fojan, E. Petersen, and G. Courtade. 2023. Biochemical Characterization and NMR Study of a PET-Hydrolyzing Cutinase from Fusarium solani pisi. *Biochemistry*. 62:1369–1375.

31. Pirillo, V., M. Orlando, D. Tessaro, L. Pollegioni, and G. Molla. 2021. An Efficient Protein Evolution Workflow for the Improvement of Bacterial PET Hydrolyzing Enzymes. *Int. J. Mol. Sci.* 23:264.

32. Schörghuber, J., L. Geist, G. Platzer, R. Konrat, and R.J. Lichtenecker. 2017. Highly Selective Stable Isotope Labeling of Histidine Residues by Using a Novel Precursor in E. coli-Based Overexpression Systems. *Chembiochem Eur. J. Chem. Biol.* 18:1487–1491.

33. Cox, N., R. Kuemmerle, P. Millard, E. Cahoreau, J.-M. François, J.-L. Parrou, and G. Lippens. 2019. Integrated pH Measurement during Reaction Monitoring with Dual-Reception 1H–31P NMR Spectroscopy. *Anal. Chem.* 91:3959–3963.

34. Vonrhein, C., C. Flensburg, P. Keller, A. Sharff, O. Smart, W. Paciorek, T. Womack, and G. Bricogne. 2011. Data processing and analysis with the autoPROC toolbox. *Acta Crystallogr. D Biol. Crystallogr.* 67:293–302.

35. McCoy, A.J., R.W. Grosse-Kunstleve, P.D. Adams, M.D. Winn, L.C. Storoni, and R.J. Read. 2007. Phaser crystallographic software. *J. Appl. Crystallogr.* 40:658–674.

36. Adams, P.D., P.V. Afonine, G. Bunkóczi, V.B. Chen, I.W. Davis, N. Echols, J.J. Headd, L.-W. Hung, G.J. Kapral, R.W. Grosse-Kunstleve, A.J. McCoy, N.W. Moriarty, R. Oeffner, R.J. Read, D.C. Richardson, J.S. Richardson, T.C. Terwilliger, and P.H. Zwart. 2010. PHENIX: a comprehensive Python-based system for macromolecular structure solution. *Acta Crystallogr. D Biol. Crystallogr.* 66:213–221.

37. Emsley, P., B. Lohkamp, W.G. Scott, and K. Cowtan. 2010. Features and development of Coot. *Acta Crystallogr. D Biol. Crystallogr.* 66:486–501.

38. Hunkapiller, M.W., S.H. Smallcombe, D.R. Whitaker, and J.H. Richards. 1973. Carbon nuclear magnetic resonance studies of the histidine residue in alpha-lytic protease. Implications for the catalytic mechanism of serine proteases. *Biochemistry*. 12:4732–4743.

39. Löhr, F., V. Katsemi, M. Betz, J. Hartleib, and H. Rüterjans. 2002. Sequence-specific assignment of histidine and tryptophan ring 1H, 13C and 15N resonances in 13C/15N- and 2H/13C/15N-labelled proteins. *J. Biomol. NMR*. 22:153–164.

40. Pelton, J.G., D.A. Torchia, N.D. Meadow, and S. Roseman. 1993. Tautomeric states of the active-site histidines of phosphorylated and unphosphorylated IIIGlc, a signal-transducing protein

from Escherichia coli, using two-dimensional heteronuclear NMR techniques. *Protein Sci. Publ. Protein Soc.* 2:543–558.

41. Shaka, A.J., P.B. Barker, and R. Freeman. 1985. Computer-optimized decoupling scheme for wideband applications and low-level operation. *J. Magn. Reson. 1969*. 64:547–552.

42. Platzer, G., M. Okon, and L.P. McIntosh. 2014. pH-dependent random coil (1)H, (13)C, and (15)N chemical shifts of the ionizable amino acids: a guide for protein pK a measurements. *J. Biomol. NMR*. 60:109–129.

43. Favier, A., and B. Brutscher. 2011. Recovering lost magnetization: polarization enhancement in biomolecular NMR. *J. Biomol. NMR*. 49:9–15.

44. Sudmeier, J.L., E.M. Bradshaw, K.E. Coffman Haddad, R.M. Day, C.J. Thalhauser, P.A. Bullock, and W.W. Bachovchin. 2003. Identification of Histidine Tautomers in Proteins by 2D ^{1}H/^{13}C$^{\delta 2}$ One-Bond Correlated NMR. *J. Am. Chem. Soc.* 125:8430–8431.

45. Semenov, V.A., D.O. Samultsev, and L.B. Krivdin. 2015. Theoretical and experimental study of 15N NMR protonation shifts. *Magn. Reson. Chem. MRC*. 53:433–441.

46. Bachovchin, W.W. 2001. Review: Contributions of NMR spectroscopy to the study of hydrogen bonds in serine protease active sites. *Magn. Reson. Chem.* 39:S199–S213.

47. Li, S., and M. Hong. 2011. Protonation, Tautomerization, and Rotameric Structure of Histidine: A Comprehensive Study by Magic-Angle-Spinning Solid-State NMR. *J. Am. Chem. Soc.* 133:1534–1544.

48. Poulsen, K.R., T. Snabe, E.I. Petersen, P. Fojan, M.T. Neves-Petersen, R. Wimmer, and S.B. Petersen. 2005. Quantization of pH: Evidence for Acidic Activity of Triglyceride Lipases. *Biochemistry*. 44:11574–11580.

49. Bhattacharya, S., and J.T. Lecomte. 1997. Temperature dependence of histidine ionization constants in myoglobin. *Biophys. J.* 73:3241–3256.

50. Hofer, F., J. Kraml, U. Kahler, A.S. Kamenik, and K.R. Liedl. 2020. Catalytic Site pKa Values of Aspartic, Cysteine, and Serine Proteases: Constant pH MD Simulations. *J. Chem. Inf. Model.* 60:3030–3042.

51. Blow, D.M., J.J. Birktoft, and B.S. Hartley. 1969. Role of a buried acid group in the mechanism of action of chymotrypsin. *Nature*. 221:337–340.

52. Ash, E.L., J.L. Sudmeier, R.M. Day, M. Vincent, E.V. Torchilin, K.C. Haddad, E.M. Bradshaw, D.G. Sanford, and W.W. Bachovchin. 2000. Unusual 1H NMR chemical shifts support (His) C(epsilon) 1...O==C H-bond: proposal for reaction-driven ring flip mechanism in serine protease catalysis. *Proc. Natl. Acad. Sci. U. S. A.* 97:10371–10376.

53. Polgár, L. 2005. The catalytic triad of serine peptidases. *Cell. Mol. Life Sci. CMLS*. 62:2161–2172.

54. Czapinska, H., and M. Bochtler. 2022. The Nε-Rule for Serine, but Not Cysteine Catalytic Triads. *Angew. Chem. Int. Ed Engl.* 61:e202206945.

55. Prompers, J.J., A. Groenewegen, C.W. Hilbers, and H.A. Pepermans. 1999. Backbone dynamics of Fusarium solani pisi cutinase probed by nuclear magnetic resonance: the lack of interfacial activation revisited. *Biochemistry*. 38:5315–5327.

56. Geierstanger, B., M. Jamin, B.F. Volkman, and R.L. Baldwin. 1998. Protonation Behavior of Histidine 24 and Histidine 119 in Forming the pH 4 Folding Intermediate of Apomyoglobin. *Biochemistry*. 37:4254–4265.

57. Yu, L., and S.W. Fesik. 1994. pH Titration of the histidine residues of cyclophilin and FK506 binding protein in the absence and presence of immunosuppressant ligands. *Biochim. Biophys. Acta BBA - Protein Struct. Mol. Enzymol.* 1209:24–32.

58. Edgcomb, S.P., and K.P. Murphy. 2002. Variability in the pKa of histidine side-chains correlates with burial within proteins. *Proteins Struct. Funct. Bioinforma.* 49:1–6.

59. Heumann, S., A. Eberl, H. Pobeheim, S. Liebminger, G. Fischer-Colbrie, E. Almansa, A. Cavaco-Paulo, and G.M. Gübitz. 2006. New model substrates for enzymes hydrolysing polyethyleneterephthalate and polyamide fibres. *J. Biochem. Biophys. Methods*. 69:89–99.

60. Badino, S.F., J.A. Bååth, K. Borch, K. Jensen, and P. Westh. 2021. Adsorption of enzymes with hydrolytic activity on polyethylene terephthalate. *Enzyme Microb. Technol.* 152:109937.

61. Rennison, A.P., A. Nousi, P. Westh, R. Marie, and M.S. Møller. Unveiling PET Hydrolase Surface Dynamics through Fluorescence Microscopy. *ChemBioChem*. n/a:e202300661.

Figure 2

Click here to access/download;Figure;Figure_2.tiff

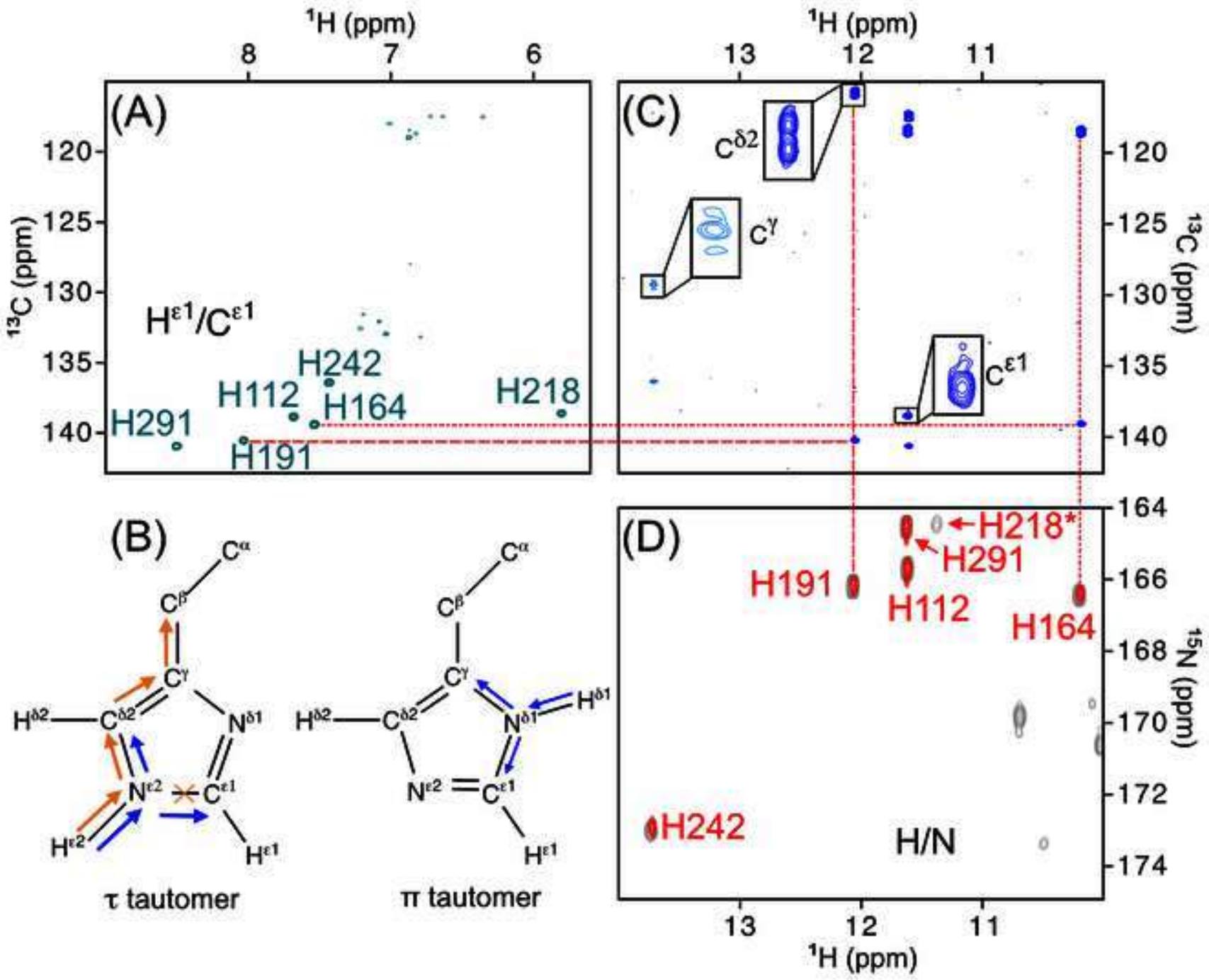

Figure 3

Click here to access/download;Figure;Figure_3.tiff

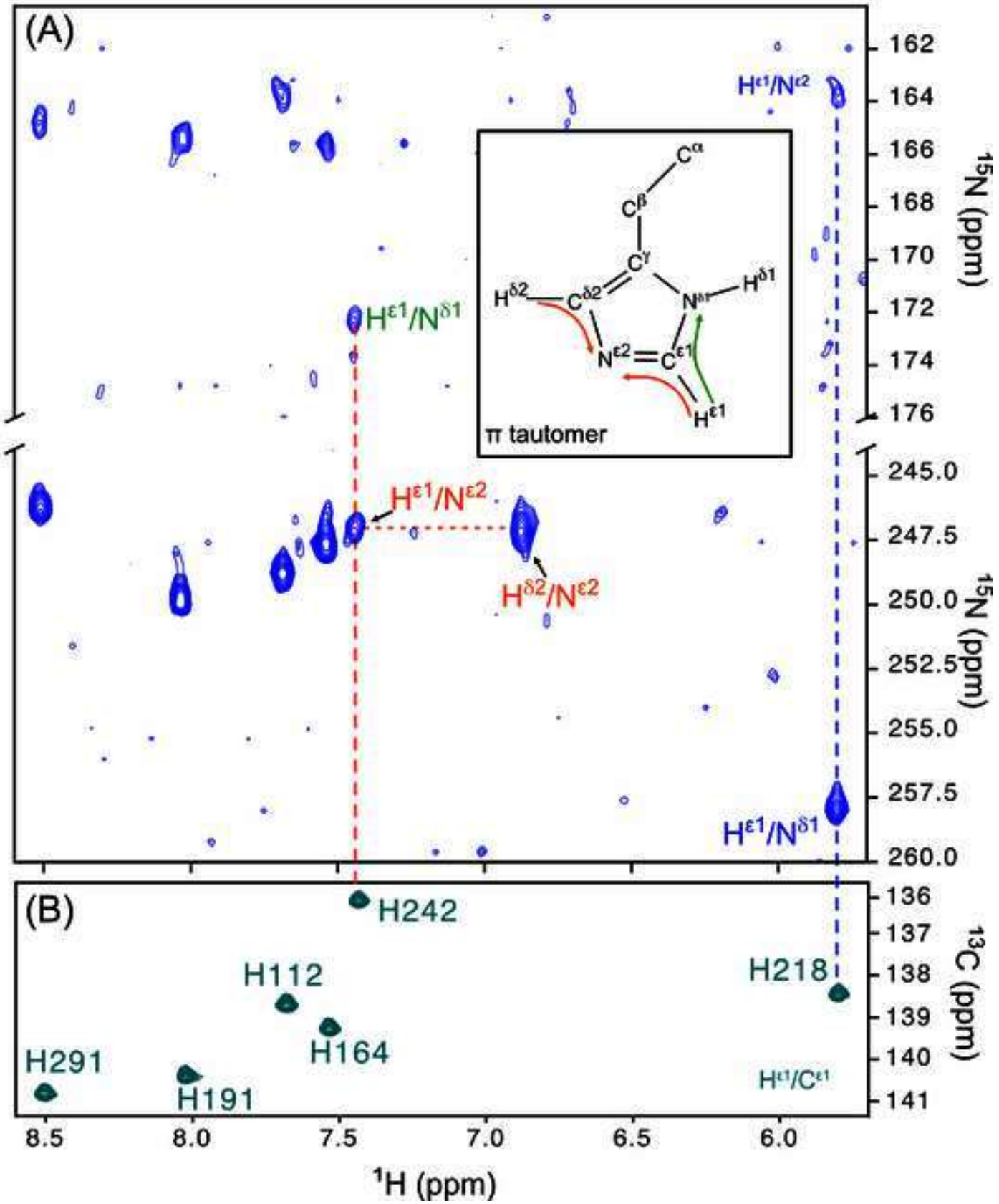

Figure 4

Click here to access/download;Figure;Figure_4.tiff

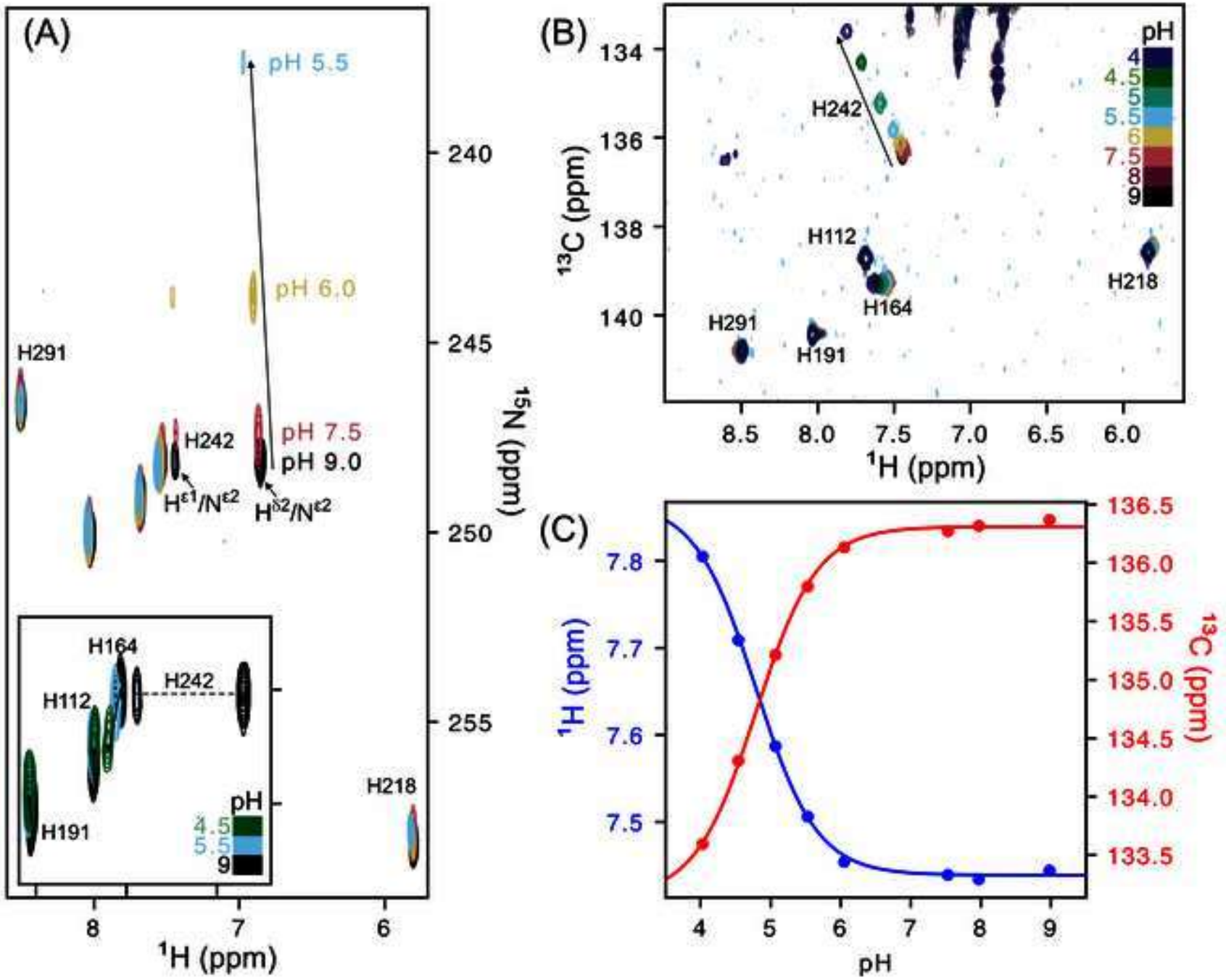

Figure 5

Click here to access/download;Figure;Figure_5.tiff

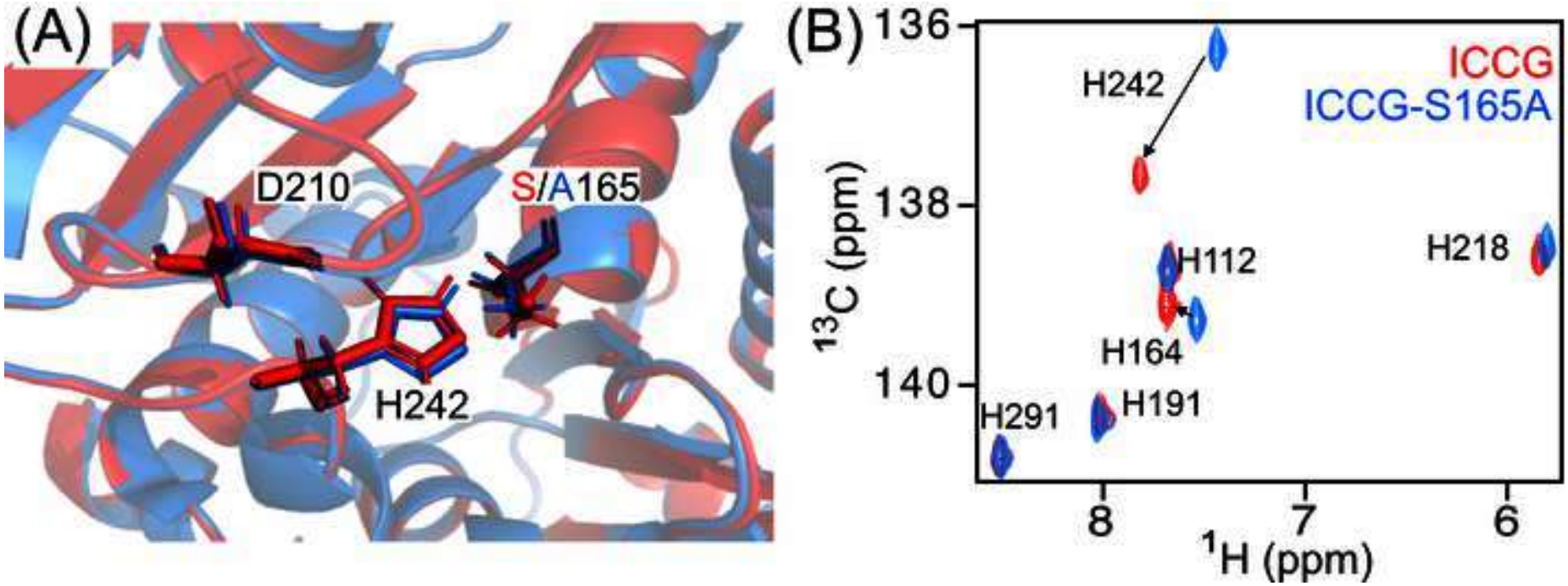

Figure 6

Click here to access/download;Figure;Figure_6.tiff

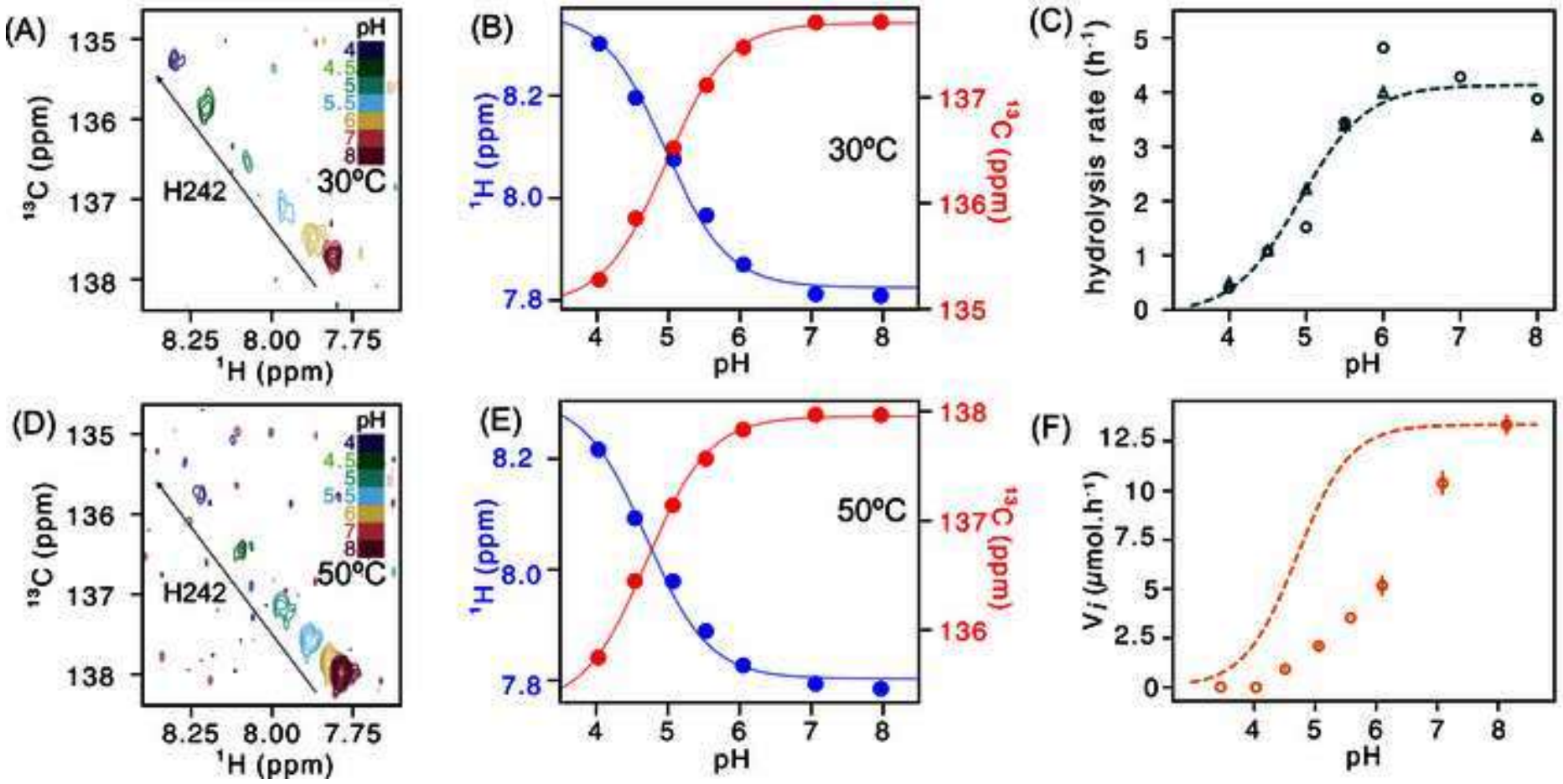

Figure 1

Click here to access/download;Figure;Figure_1.tiff

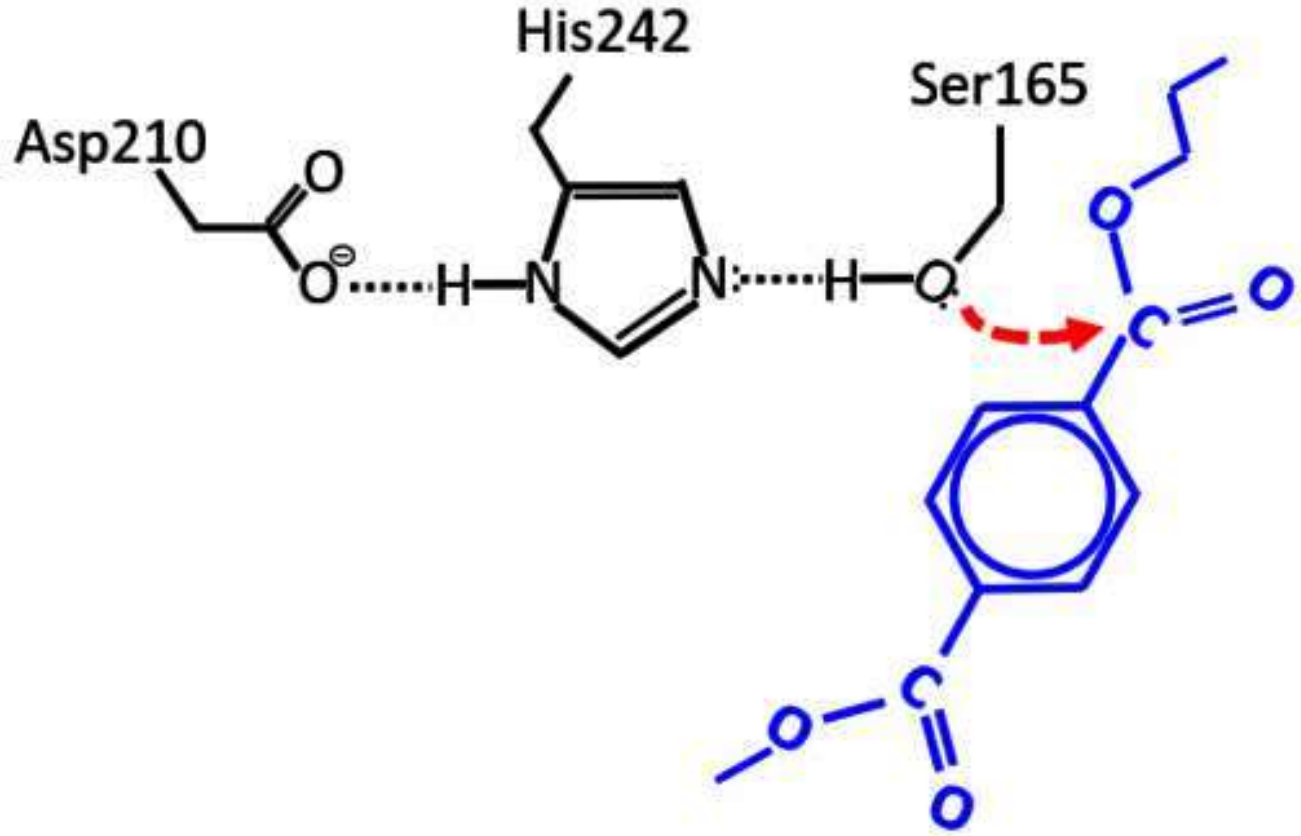

Supplemental Information

Click here to access/download
Supplemental Information
SI_210424.pdf